

Radio Spectral Evolution of an X-ray Poor Impulsive Solar Flare: Implications for Plasma Heating and Electron Acceleration

T. S. Bastian

G. D. Fleishman¹

National Radio Astronomy Observatory, Charlottesville, VA 22903

D. E. Gary

New Jersey Institute of Technology, Newark, NJ

ABSTRACT

We present radio and X-ray observations of an impulsive solar flare that was moderately intense in microwaves, yet showed very meager EUV and X-ray emission. The flare occurred on 2001 Oct 24 and was well-observed at radio wavelengths by the Nobeyama Radioheliograph (NoRH), the Nobeyama Radio Polarimeters (NoRP), and by the Owens Valley Solar Array (OVSA). It was also observed in EUV and X-ray wavelength bands by the TRACE, GOES, and *Yohkoh* satellites. We find that the impulsive onset of the radio emission is progressively delayed with *increasing* frequency relative to the onset of hard X-ray emission. In contrast, the time of flux density maximum is progressively delayed with *decreasing* frequency. The decay phase is independent of radio frequency. The simple source morphology and the excellent spectral coverage at radio wavelengths allowed us to employ a nonlinear χ^2 -minimization scheme to fit the time series of radio spectra to a source model that accounts for the observed radio emission in terms of gyrosynchrotron radiation from MeV-energy electrons in a relatively dense thermal plasma. We discuss plasma heating and electron acceleration in view of the parametric trends implied by the model fitting. We suggest that stochastic acceleration likely plays a role in accelerating the radio-emitting electrons.

Subject headings: Sun: flares — Sun: radio radiation — Sun: X-rays — acceleration of particles

¹Ioffe Institute for Physics and Technology, St. Petersburg, Russia

1. Introduction

Radio and X-ray radiation from solar flares have been used for many years to study energy release, plasma heating, and particle acceleration and transport. Joint studies of radio and X-ray radiation are particularly powerful because they probe populations of electrons at different energies, ranging from hot thermal electrons to nonthermal electrons of tens of keV emitting at soft X-ray (SXR) and hard X-ray (HXR) wavelengths, and nonthermal electrons with energies ranging from hundreds of keV to several MeV emitting γ -rays and centimeter- and millimeter-wavelength radiation (e.g., Takakura et al. 1983; Klein et al. 1986; Bruggmann et al. 1994; Ramaty et al. 1994, Trotter et al. 1998, 2002). Flares are conveniently divided into two broad classes, impulsive (or compact) and gradual (or extended) flares (Pallavicini et al. 1977) although more complex classification schemes have been proposed (e.g., Bai & Sturrock 1989) in response to more detailed and comprehensive observations. Impulsive flares tend to occur in relatively high density, compact, coronal magnetic loops, and display a good correlation between the microwave and HXR emission (Kai et al. 1985, Kosugi et al. 1988). Gradual events tend to occur in lower density, larger scale coronal loops, emitting for significantly longer times. They tend to be “microwave rich” (Bai & Dennis 1985) by a factor of ~ 5 compared to the microwave-HXR correlation of impulsive events (Kosugi et al. 1988). The spectral and temporal profiles of these two classes also follow a predictable evolution (e.g. Silva et al. 2000). Impulsive bursts show a soft-hard-soft spectral evolution in hard X-rays and a radio peak-frequency evolution that evolves from low to high, and often back to low (Melnikov et al. 2007). Gradual bursts, in contrast, show a soft-hard-harder evolution in X-rays and a radio spectral peak that is often constant or slowly increasing in frequency with time. Bursts that do not obey these general rules are often worthy of detailed study, especially when well observed, in order to test our understanding of the underlying physical mechanisms.

The impulsive flare of 2001 October 24 at 23:10 UT is an example of such a burst, which was well observed by a broad suite of instrumentation operating at radio and X-ray wavelengths and therefore offers an opportunity to study a wide range of electron energies. The event stands out paradoxically as an extremely X-ray-poor impulsive flare, producing a moderately intense radio burst, yet very little EUV, SXR, or HXR emission. It is similar in several respects to a radio burst studied by White et al. (1992), an event for which available radio data suggested that energy release occurred in a dense plasma ($n_e \sim 5 \times 10^{11} \text{ cm}^{-3}$). Veronig & Brown (2004) have identified a class of HXR sources that also occur in a relatively dense plasma ($n_e \approx 1 - 2 \times 10^{11} \text{ cm}^{-3}$). As we show here, the Oct. 24 event is another example of an event in which energy release occurs in a dense plasma. However, unlike the events studied by Veronig & Brown, the Oct. 24 event is highly impulsive; and unlike the event discussed by White et al., the Oct. 24 event shows significant radio spectral

evolution. Although the physical conditions and the evolution of the burst are unusual, we believe that the physical processes are not. The excellent observational coverage at radio and X-ray wavelengths provides us with the opportunity to address electron acceleration in a dense plasma environment in some detail. In particular, the excellent time-resolved radio spectroscopic data available from OVSA and the NoRP has allowed us to fit the data to a source model as a function of time and thereby deduce the time variation of source parameters. These, in turn, have yielded insights into the nature and consequences of energy release in a dense plasma.

The paper is organized as follows: In §2 we present the radio, EUV, and X-ray observations of the flare. In §3 we argue that the data may be understood in terms of fast electrons injected into a relatively cool, dense magnetic loop. We explicitly fit a time series of radio spectroscopic data to a simple model that embodies these assumptions using a nonlinear χ^2 minimization scheme. The parametric trends to emerge show that the time series of spectra is well fit if the temperature of the ambient plasma increases in time. We discuss implications of the model fits for plasma heating, electron acceleration, and electron transport in §4. We suggest that the lack of significant X-ray emission can be understood if the magnetic mirror ratio is large, thereby suppressing electron precipitation and reducing conduction at the foot points. The relatively high plasma density in the source renders it collisionally thick to electrons with energies of some 10s of keV. We argue that collisional heating yields the systematic plasma heating inferred from model fitting. Furthermore, electrons are accelerated progressively to energies exceeding MeV energies over over a time scale < 10 s. We suggest that stochastic processes may play a significant role in the acceleration and transport of electrons. We conclude in §5.

2. Observations

The flare on 2001 October 24 occurred in NOAA active region 9672 at a heliocentric position of S18W13 from approximately 23:10-23:14 UT. AR 9672 was in a $\beta\gamma\delta$ magnetic configuration and had produced M and X class soft X-ray flares in previous days. While the relatively strong radio event from AR9672 was noted by the NOAA Space Environment Center, it was incorrectly associated with an H α subflare that occurred nearly concurrently, from 23:07-23:12 UT, in AR 9678 (N06E33). No H α observations of AR 9672 are available at the precise time of the event. While no soft X-ray emission was noted by NOAA/SEC from either the H α subflare in AR9678 or the radio burst in AR9672, weak extreme-ultraviolet (EUV), soft X-ray (SXR), and hard X-ray (HXR) emissions were in fact detected from the flare in AR9672 by the *Transition Region and Coronal Explorer* (TRACE; Handy et al. 1999),

the *Yohkoh* Soft X-ray Telescope (SXT), and Hard X-ray Telescope (HXT), respectively (Kosugi et al. 1992), as was a weak SXR enhancement by the GOES 10 satellite. The radio burst was well-observed in total intensity by the Owens Valley Solar Array (OVSA; Gary & Hurford 1994), the Nobeyama Radio Polarimeters (NoRP), and by the Nobeyama Radioheliograph (NoRH; Nakajima et al. 1994).

Fig. 1a provides an overview of selected X-ray and radio observations. The HXR and radio light curves show a simple, highly impulsive rise and exponential decay over a duration of approximately 4 min whereas the GOES SXR bands decay to half their peak flux on a time scale < 10 min. The horizontal line at the top of Fig. 1a indicates the time range shown in Fig. 1b. Here, the HXR light curve is shown with the NoRP frequencies. We now discuss the EUV, X-ray, and radio observations in greater detail.

2.1. General Comparison of NoRP and HXT L band Events

To place the 2001 October 24 event in the broader context of events jointly observed in the radio and HXR bands, Fig. 2 shows a scatter plot of the 135 flares observed jointly by the NoRP at 17 GHz and the HXT L band during the lifetime of the *Yohkoh* mission. Analogous figures have compared the 17 GHz peak flux with the HXR counts from the hard X-ray spectrometer on board *Hinotori* (Kai et al. 1985) and from the HXRBS experiment on board the *Solar Maximum Mission* (Kosugi et al. 1988). As in these previous examples, there is a clear correlation between the peak 17 GHz flux and the peak HXT L band count rate. The Spearman (rank) correlation coefficient is 0.57, and the two-sided significance of the correlation – i.e., the probability that the correlation coefficient is larger than this value in the null hypothesis – is essentially zero, indicating the correlation is highly significant. The flare of 2001 October 24 has a peak flux of 425 SFU¹ at 17 GHz. The regression curve implies that an HXT L band count rate of more than 200 cts s⁻¹ sc⁻¹ is expected, yet a peak count rate of only 7 cts s⁻¹ sc⁻¹ is measured (including a background of ≈ 1 ct s⁻¹ sc⁻¹). The flare is X-ray poor by a factor of ~ 30 relative to the regression curve. We use the term “X-ray poor” rather than “microwave rich” because, as noted in the Introduction, the latter term is associated with gradual events showing excess microwave emission (Bai & Dennis 1985, Cliver et al. 1986, Kosugi et al. 1988).

¹1 solar flux unit = 10^{-22} W m⁻² Hz⁻¹

2.2. EUV and X-ray Observations of the Oct 24 Event

While the Oct 24 event is very X-ray poor it was nevertheless detected by several instruments operating at EUV and X-ray wavelengths. It was imaged by TRACE in the 171 Å band with a cadence of ≈ 40 s and an angular resolution of $1''$. An image was obtained just prior to the impulsive rise at 23:10:46 UT and another was obtained at 23:11:26 UT (Fig 1b). A difference image formed from the latter image and one obtained at 23:10:05 UT reveals discrete kernels of emission (Fig. 3a).

In soft X-rays, the GOES 10 background level was approximately C2.3 and the enhancement above background was approximately B2. The X-ray emission was too weak to trigger flare mode observing by the SXT. As a result, only one low-resolution ($4.92''$) full-disk SXR image (AlMg filter) is available during this brief impulsive flare, at 23:11:46 UT (Fig 1b, Fig. 3b).

The *Yohkoh* HXT typically observed flares in four photon energy bands – L (13.9-22.7 keV), M1 (22.7-32.7 keV), M2 (32.7-52.7 keV), and H (52.7-92.8 keV). In this case, however, the HXT flare mode was not triggered and counts were therefore recorded in L band only. The L band light curve (Fig. 1) shows a simple impulsive spike with a maximum background-subtracted count rate of only $6 \text{ cts s}^{-1} \text{ sc}^{-1}$ and a FWHM duration of just 18 s. Integrating over the full duration of the event yields sufficient counts to image the HXR source with an angular resolution of $\approx 5''$ (Fig. 3c).

The *Yohkoh* Wide-band Spectrometer (WBS; Yoshimori et al. 1992) may have made a marginal detection in energy channels up to 50 keV (H. Hudson, private communication) but given uncertainties in the calibration the implications for the HXR photon spectrum are highly uncertain. We therefore do not consider WBS data here.

Each of the maps shown in Fig. 3 is compared with a magnetogram. The flare is associated with a magnetic bipole just south of the dominant sunspot group in AR 9672. The length of the source is $\approx 30''$ in SXR and its width is $\approx 12''$. The SXR and HXR sources are coincident (cf. Veronig & Brown 2004) and are consistent with a magnetic loop or unresolved loops, the latter suggested by the discrete kernels seen in the TRACE 171 Å emissions, presumed here to be footpoint emission.

2.3. Radio Observations of the Oct 24 Event

Radio imaging observations of the flare were obtained by the NoRH at 17 and 34 GHz. The NoRH observations were made early in the day, local time, and the angular resolution

was therefore reduced in one dimension, yielding an elliptical beam of approximately $24'' \times 10''$ at 17 GHz, and $13'' \times 5''$ at 34 GHz, both with a position angle $\phi \approx -40^\circ$. Figs. 4a and 4c show the 17 and 34 GHz maps in total intensity (Stokes I) overlaid on the magnetogram. The source morphology evolves very little at radio wavelengths as a function of time; we therefore show maps near the time of maximum intensity. The peak brightness temperature of the 17 GHz source is 4.6×10^7 K whereas that of the 34 GHz source is 1.8×10^7 K. Fig. 4b shows the 17 GHz map of the circularly polarized flux (Stokes V parameter) superposed on the magnetogram, demonstrating that it is polarized in the sense of the x-mode with right-circularly polarized emission associated with positive magnetic polarity. The degree of circular polarization (I/V) ranges from 20% left-circularly polarized (LCP; negative values of Stokes V) to 10% right-circularly polarized (RCP; positive values of Stokes V). The observed change in the sense of circular polarization along the length of the loop from RCP to LCP reflects the reversal of magnetic polarity while the asymmetry in the degree of RCP/LCP polarization indicates an asymmetry in the magnitude of the positive and negative magnetic polarity. The sources observed in the SXR, HXR, and radio bands are coincident and quite similar in morphology. All imaging data are consistent with the illumination of a simple magnetic loop, or unresolved bundle of loops, straddling a magnetic neutral line. We note that the loop is not visible in the NoRH 17 and 34 GHz maps as a discrete feature in the active region prior to the flare. We estimate the 17 GHz brightness temperature prior to the flare is $\sim 10^5$ K.

The NoRP measures the total solar flux in Stokes I and V at frequencies $\nu = 1, 2, 3.75, 9.4, 17, 35$, and 80 GHz. Referring to the NoRP observations summarized in Fig. 1b, we note several features. First, the onset of the 35 GHz emission is delayed by ≈ 3 s relative to that at 17 GHz which is, in turn, delayed by ≈ 3 s relative to the onset of the HXT L band emission. Second, the time of the 17 GHz flux maximum is delayed by ≈ 3 s relative to that at 35 GHz and the maximum of the 9.4 GHz light curve is delayed by 12 s relative to that at 17 GHz. Note, however, that a “shoulder” in the 9.4 GHz emission roughly coincides with the 17 and 35 GHz maxima, a point discussed further in §4. Third, the decay profiles of the 9.4, 17, and 35 GHz light curves are nearly identical and are exponential after approximately 23:11:20 UT with a decay time of ≈ 48 s. Fourth, there is no detectable radio emission at 3.75 GHz. Finally, while the flare was detected at 80 GHz the signal is very noisy ($4-5\sigma$). We note that both the sensitivity and the calibration of the 80 GHz flux on this date are rather poor, the absolute flux calibration being no better than $\approx 40\%$ (H. Nakajima, private communication).

These features are confirmed and extended by the OVSA observations. On 2001 October 24, OVSA employed a high cadence observing mode to produce 24 point spectra between 1.2-14.8 GHz every 2 s in total intensity. A detail of the impulsive onset of the flare is shown

in Fig. 5a which plots the HXT L band data, three OVSA frequencies (11.2, 12.4, and 14.8 GHz, labeled with a prefix “O”), and three NoRP frequencies (9.4, 17, and 35 GHz, labeled with a prefix “N”) for a period of 20 s. The frequencies 12.4, 14.8, 17, and 35 GHz show a progressive delay in their flux onset relative to the HXT L band emission. The onset of emission at 9.4 and 11.2 GHz show the opposite pattern, however. These trends are also clearly seen in the dynamic spectrum of the OVSA data (Fig. 6). For frequencies $\gtrsim 12$ GHz the flux onset is increasingly delayed with frequency whereas the opposite trend is seen for $\nu \lesssim 12$ GHz.

Fig. 5b shows a detail of the decay phase for the same selection of frequencies shown in Fig. 5a. Each frequency has been scaled so that for times later than 23:11:20 UT the light curves are overlaid, showing that the exponential decay from 9.4 to 35 GHz is essentially identical after 23:11:20 UT. Fig. 5b also illustrates the progressive delay of the flux maximum with decreasing frequency. This feature is more clearly illustrated in Fig. 6, in which it is readily seen (dashed line) that the time of the flux maximum increases with decreasing frequency. There is no detectable emission below $\sim 5 - 6$ GHz.

The radio spectral evolution of the flare is summarized in Fig. 7, which shows composite spectra using OVSA data (plus symbols) and NoRP data (diamonds) during the impulsive rise and exponential decay. The spectral maximum is near 17 GHz during the rise phase but declines to ~ 10 GHz during the decay phase.

2.4. Observational Summary

Given the rather extensive data set it is useful to consolidate and summarize our findings regarding the flare on 2001 October 24:

- The flare is one of the most X-ray poor events of those jointly observed by the NoRP and *Yohkoh* HXT.
- The NoRH 17 and 34 GHz images, and the *Yohkoh* SXT and HXT L band images are all coincident and similar in morphology. The source is consistent with a simple magnetic loop or unresolved bundle of loops. The TRACE 171Å difference image reveals small kernels consistent with loop foot points.
- Due to the paucity of X-rays, the photon spectrum was not measured and the electron spectrum is therefore unconstrained by HXR emission.
- The observed radio emission is relatively strong and the spectral coverage is excellent, allowing the following observations to be made:

- Radio emission is detected up to 80 GHz. The spectral maximum is ~ 17 GHz during the impulsive rise, declining to ~ 10 GHz during its decay. Radio emission is undetectable below $\sim 5 - 6$ GHz.
- The impulsive onset of emission shows a progressive delay with *increasing* frequency for $\nu \gtrsim 12$ GHz; the trend reverses below ≈ 12 GHz.
- In contrast, the time of absolute flux maximum shows a progressive delay with *decreasing* frequency for all frequencies measured.
- For times later than approximately 23:11:20 UT the decay profile of the radio emission is independent of frequency over two octaves and is characterized by a decay time of ≈ 48 s.

Despite the relatively simple source morphology in the X-ray and radio bands, and the single impulsive spike shown in the HXR and radio light curves, this event displays considerable spectral richness at radio wavelengths. In the next section we develop a source model and perform parametric fits to the time series of radio spectra. The parametric trends to emerge from these fits then guide our physical interpretation of the event in §4.

3. Model of the Radio Source

We now direct our attention to the well-observed radio source and fit a simple model to the radio data as a function of time. A fully self-consistent, three dimensional, time-dependent, inhomogeneous model of the source is beyond the scope of this work. We instead account for the essential features of the source in terms of a magnetized volume containing thermal plasma and energetic electrons. Similar models have been developed to account for the spectral (e.g., Klein 1987; Benka & Holman 1992; Bruggmann et al. 1994), temporal (e.g., Bruggmann et al. 1994), or spatial (Bastian et al. 1998; Nindos et al. 2000; Kundu et al. 2004) properties of radio observations. Typically, these efforts have been strongly under-constrained in the temporal, spatial, and/or spectral domains. Moreover, model fitting has typically been limited to adjusting model parameters until a reasonable fit by eye is obtained.

In the present case, we have comparatively good spectral and temporal coverage of the event at radio wavelengths. While imaging data are limited, the source is apparently rather simple. It is therefore possible to make simplifying assumptions regarding the source volume and to exploit nonlinear optimization techniques to fit the observed radio spectrum. Moreover, such fits can be performed on the time series of spectra, from which the time variation of fitted parameters can be deduced. As such, the fitting represents a means of time-resolved radio-spectral inversion. While the model is admittedly crude, it nevertheless

allows us to identify trends in the time variation of critical parameters in an unbiased fashion. In other words, rather than postulating a time dependence for physical parameters of interest, the time dependence emerges from the model fits. In this section we describe the model and the underlying assumptions, explore the parametric dependencies of the model, and then present the fitting scheme and the results derived from the fits in detail.

3.1. Model and Assumptions

We assume the observed radio emission is the result of gyrosynchrotron radiation from energetic electrons in a magnetic loop. A striking feature of the radio spectra is the relatively steep roll-off in the emission below 10 – 17 GHz, with no emission detectable at all below ≈ 6 GHz, a feature that persists for the duration of the event. The spectrum of the radio emission is clearly nonthermal, yet the brightness temperature of the 17 and 34 GHz sources is unexceptional, characteristic of optically thin emission. We therefore suggest that the Razin effect (Razin 1960, Ginzburg & Syrovatskii 1969) plays a role in this flare. The Razin effect suppresses gyrosynchrotron emission in the presence of an ambient plasma below a cutoff frequency $\nu_R \approx \nu_{pe}^2/\nu_{Be} \approx 20n_{th}/B$, where n_{th} is the thermal electron density and B is the source magnetic field. For $\nu_R \sim 10 - 17$ GHz and an ambient density $n_{th} \sim 10^{11} \text{ cm}^{-3}$, $B = 120 - 200$ G. For a given cutoff frequency ν_R , higher magnetic field strengths require higher thermal electron densities.

The thermal free-free absorption coefficient at radio wavelengths is $\kappa_{ff} \approx 0.2n_e^2T^{-3/2}\nu^{-2}$ for coronal conditions (Dulk 1985). The optical depth τ_{ff} through a plasma layer L is $\tau_{ff} = \kappa_{ff}L$. Substituting plausible values for the relevant parameters – $T = 2 \times 10^6$ K, $L = 5 \times 10^8$ cm, and $n_{th} = 10^{11} \text{ cm}^{-3}$ – we find that $\tau_{ff} \approx 350\nu_9^{-2}$, where ν_9 is the frequency in GHz. The optical depth is even larger for cooler plasma. It is clear that if Razin suppression is important, free-free absorption is, too. Consequently, we assume that Razin suppression and free-free absorption each play a role in determining the shape of the radio spectrum and include both in our model calculations (cf. Ramaty & Petrosian 1972, Klein 1987).

As previously noted, the source morphology changes little during the event. We therefore consider a homogeneous source with an area $A = 2 \times 10^{18} \text{ cm}^2$ ($12'' \times 30''$) and a depth $L = 9 \times 10^8$ cm ($12''$), consistent with the X-ray and radio imaging (see §2.4). The source volume is assumed to contain thermal plasma with a density n_{th} and a temperature T , permeated by a coronal magnetic field B with an angle θ relative to the line of sight. Finally, it is assumed that an isotropic, power-law distribution of energetic electrons $N(E)dE = KE^{-\delta}dE$ is uniformly mixed with the thermal plasma, with a normalization energy E_o and a high-

energy cutoff energy E_c . The total number density of nonthermal electrons between E_o and E_c is n_{rl} . No electron transport effects are explicitly included in the model calculation.

The computation of radio emission from even as simple a source model as this depends on many parameters. To make further progress, additional assumptions are necessary. First, we assume the magnetic field remains constant for the duration of the event. However, as a means of estimating the dependence of the fitted parameters on the magnetic field, different values of the magnetic field were assumed for different fitting runs. Second we assume the number density of the background thermal plasma also remains constant. In fact, as discussed further in §3.3, preliminary fits allowed n_{th} to vary but the fitted values showed little variation with time. Hence, it was typically held fixed. An additional justification for this second assumption is that, given the weak EUV and HXR emission, there was little deposition of energy near the loop footpoints and hence, little evaporation of plasma into the coronal loop. The incremental increase in density due to evaporation is therefore presumed to be small. We do allow the temperature of the thermal background plasma to vary with time, however. Finally, we note that the radio emission is insensitive to E_o and therefore set it equal to 100 keV.

To summarize, we model the radio source as a simple homogenous volume with an area A and a depth L . The volume is filled with a thermal plasma with a number density n_{th} and is permeated by a magnetic field B oriented at an angle θ to the line of sight; n_{th} , B , and θ are assumed to be constant during the flare but the plasma temperature is allowed to vary. A power-law distribution of n_{rl} energetic electrons per cubic centimeter between energies E_o and E_c is uniformly mixed with the background plasma. The electron pitch angle distribution is assumed to be isotropic. Typically two or three out of four parameters – n_{rl} , T , E_c , and δ – were allowed to vary in fitting the data to the model.

3.2. Model Dependencies

It is useful to make a brief aside at this point to outline the computation of the radio emission spectrum and to elucidate the dependencies of the computed spectrum on various parameters of interest. For the homogeneous source described above, the source flux at a given frequency is computed as (Ramaty & Petrosian 1972; Benka & Holman 1992)

$$S(\nu, B, \theta, T, n_{th}, E_o, E_c, n_{rl}, \delta) = 2k_B \frac{\nu^2}{c^2} \frac{1}{\mu^2(\nu, n_{th}, B, \theta)} \frac{j_T}{\kappa_T} \frac{A}{D^2} [1 - \exp(-\kappa_T L)] \quad (1)$$

where $\mu(\nu, n_{th}, B, \theta)$ is the index of refraction, $j_T = j_{ff}(\nu, T, n_{th}) + j_{gs}(\nu, B, \theta, n_{th}, n_{rl}, E_o, E_c, \delta)$

is the total emissivity due to the free-free and gyrosynchrotron mechanisms, $\kappa_T = \kappa_{ff}(\nu, T, n_{th}) + \kappa_{gs}(\nu, B, \theta, n_{rl}, E_o, E_c, \delta)$ is the total absorption coefficient, A/D^2 is the solid angle subtended by the source, and D is the distance from the observer to the source (1 AU).

The thermal free-free emission and absorption coefficients used for the computation of the source function are readily calculated (e.g., Lang 1980); those for gyrosynchrotron emission and absorption are more problematic. The expressions for the emissivity and absorption coefficient given by Ramaty (1969), or variants thereof (e.g., Benka & Holman 1992), are cumbersome and their calculation is computationally intensive. For the iterative χ^2 minimization scheme we employ, it is far more efficient to use the approximate expressions derived by Klein (1987) which include the effects of Razin suppression and are quite accurate for radio frequencies greater than the first few harmonics of the electron gyrofrequency ($\nu \gg \nu_B = eB/2\pi m_e c$) and for values of θ that are not too small ($> 30^\circ$).

Fig. 8 shows model spectra calculated for various sets of parameters. All four panels show a reference spectrum (solid line) due to gyrosynchrotron emission from electrons *in vacuo* ($n_{th} = 0$). The parameters used for the reference spectrum are: $B = 150$ G, $\theta = 60^\circ$, $n_{rl} = 5 \times 10^6$ cm $^{-3}$, $E_o = 100$ keV, $E_c = 2.5$ MeV, $\delta = 3$, $A = 2 \times 10^{18}$ cm 2 , and $L = 9 \times 10^8$ cm. In Fig. 8a the dashed lines indicate spectra where the source parameters are identical to those used to compute the reference spectrum except that an ambient thermal plasma is present in the source. The ambient plasma has a temperature of 2×10^6 K and its density varies from $n_{th} = 2 \times 10^{10}$ cm $^{-3}$ to 5×10^{11} cm $^{-3}$. The combined action of free-free absorption and Razin suppression strongly reduces the radio emission below 10-20 GHz for values of $n_{th} > 5 \times 10^{10}$ cm $^{-3}$. Moreover, as the density increases, the high-frequency emission is enhanced. This enhancement is entirely due to the thermal free-free contribution.

In Fig. 8b, the temperature is again $T = 2 \times 10^6$ K and the ambient density is held fixed at $n_{th} = 10^{11}$ cm $^{-3}$. Here, the magnetic field strength is allowed to vary from $B = 150$ to 350 G. All other source parameters are identical to those used to compute the reference spectrum. Note that, in contrast to gyrosynchrotron emission in which Razin suppression plays no role, the spectral maximum is insensitive to B although the peak flux increases with B .

In Fig. 8c, the density is again held fixed at $n_{th} = 10^{11}$ cm $^{-3}$, $B = 150$ G, but the plasma temperature now varies from $T = 10^6$ to 2×10^7 K. All other parameters are again the same as those used to compute the reference spectrum. For cool plasma, the combination of Razin suppression and thermal absorption strongly reduces the microwave emission. As the temperature of the ambient plasma increases, all other parameters held fixed, the microwave emission increases at lower frequencies because the free-free absorption drops as the temperature increases, but decreases at the highest frequencies owing to the correspond-

ing decrease of the optically thin free-free opacity, and the spectral maximum moves toward lower frequencies. At high enough temperatures the plasma becomes optically thin to free-free absorption ($\sim 10^7$ K in this example) and the spectrum becomes insensitive to further increases in temperature except the extreme low-frequency end of the spectrum where the emission is due to optically thick thermal radiation of the plasma and is proportional to its temperature.

Finally, in Fig. 8d, the thermal plasma density is held fixed ($n_{th} = 10^{11} \text{ cm}^{-3}$), $T = 2 \times 10^6$ K, $B = 150$ G, and the number of energetic electrons n_{rl} between E_o and E_c , varies from 10^6 to $2 \times 10^7 \text{ cm}^{-3}$. All other parameters are the same as those used to compute the reference spectrum. The microwave flux varies with n_{rl} but the spectral maximum is insensitive to variations in n_{rl} . This point has also been made by Belkora et al. (1997), Fleishman & Melnikov (2003), and Melnikov et al. (2007). The optically thin slope steepens with increasing n_{rl} as the influence of the dense thermal plasma becomes relatively less important. At low values of n_{rl} the contribution of free-free emission is significant and acts to flatten the spectrum.

While the source model is relatively simple, it yields a wide variety of spectral shapes which, in turn, yield insight to the source parameters. We now turn to fitting this simple source model to the observed data.

3.3. Model Fitting and Results

The excellent radio spectroscopic and temporal coverage of this event allow us to fit the observed radio spectra as a function of time. Lee & Gary (2000) used a similar approach to fit an electron transport model to OVSA data although a different "goodness of fit" parameter was optimized. Here, we have developed a nonlinear code that adjusts model parameters to minimize the χ^2 statistic using the downhill simplex method (Press et al. 1986). The χ^2 statistic is computed as

$$\chi^2 = \frac{1}{N - n} \sum_{i=1}^N \frac{(S_i^{obs} - S_i^{mod})^2}{\sigma_i^2} \quad (2)$$

where S_i^{obs} is the flux density at frequency i observed by either OVSA or the NoRP, S_i^{mod} is the corresponding model value, σ_i^2 is the estimated variance of the observed value, N is the number of data points, and n is the number of free parameters. The signal variance σ_i^2 at each frequency is empirically known prior to the flare. It is the result of receiver noise, the sky (35 and 80 GHz), and the Sun itself. Radio emission from the flare makes an additional

contribution that can be estimated from the known intensity of the signals and the properties of the instrument.

We have fit the model to composite radio spectra observed by OVSA (5-14.8 GHz) and the NoRP (17, 35, and 80 GHz). Data points below 5 GHz are ignored because they contain no signal. Inspection of the spectra indicates a probable systematic calibration error between the two instruments with a magnitude of $\approx 10 - 20\%$ (Fig. 8). The time resolution of the NoRP data points were averaged to 2 s to match the time resolution of the OVSA data. A total of 25 spectra were fit to data sampled between 23:10:54 and 23:11:44 UT, as indicated in Fig. 1b. The spectra at earlier and later times had insufficient signal-to-noise ratios at too many points to yield reliable fits.

While the spectral coverage of this event at radio frequencies is excellent, it is nevertheless insufficient to allow unique sets of parameters to be established from fits to the data. Excluding frequencies below 5 GHz, we fit to only sixteen data points for each time average. Indeed, as explained in §3.1, many of the source parameters are held constant and only two or three out of four parameters were varied. Clearly, the models resulting from this procedure, while providing good fits to the data, are non-unique. We set those parameters that remain constant for all fits to values we judge to be reasonable, but are fully aware that other, similar, values may in fact yield fits that are consistent with the data. We therefore consider the fits and the trends that emerge from the time series of fitted parameters to be qualitative guides in our physical interpretation of the flare in §4.

Fig. 9 shows the results of two- and three-parameter fits to the 25 spectra observed from 23:10:54 to 23:11:44 UT. In the two-parameter fit (solid line), only the number of fast electrons, n_{rl} , and the plasma temperature, T , were allowed to vary and the spectral index and cutoff energy were held fixed, with $\delta = 3.5$ and $E_c = 2.5$ MeV, respectively, as were all other relevant parameters: $B = 165$ G, $\theta = 60^\circ$, $E_o = 100$ keV, $A = 2 \times 10^{18}$ cm², and $L = 9 \times 10^8$ cm. The value for the spectral index is entirely consistent with previous findings (e.g., Ramaty et al. 1994, Trotter et al. 1998, 2000; Lüthi et al. 2004). Three parameter fits are also shown, the third parameter being either δ (dashed line) or E_c (dotted line). As discussed in §3.1, little improvement was seen in the (three-parameter) fits when the thermal plasma density, n_{th} was free to vary. The fitted value of n_{th} remained nearly constant ($n_{th} \approx 10^{11}$ cm⁻³) in all cases and was therefore held fixed at this value for the fits shown in Fig. 9. When δ was allowed to vary it, too, remained relatively constant or in some cases showed a tendency to smaller values; i.e., spectral hardening. When E_c was allowed to vary, best fit values during the rise phase of the flare yielded $E_c \approx 2$ MeV whereas for times later than approximately 23:11:12 UT, larger values of E_c resulted ($E_c \geq 10$) MeV. We note that the fits become insensitive to the precise value of E_c when it exceeds ~ 10 MeV because

the high frequency radio data most sensitive to E_c are sparse and, in the case of 80 GHz, poorly calibrated.

Fig. 10 shows a comparison between the fitted values for n_{rl} and T resulting from the two-parameter fits and the radio and HXR emission as a function of time. We note that the three-parameter fits yield similar results for the time variation of n_{rl} and T . The shaded area in each panel indicates the range of fitted values that result from varying the magnetic field strength. The time variation of n_{rl} and T are shown for three fixed values of the magnetic field (150, 165, and 180 G). Two points can be made about the apparent trends: First, the total number of energetic electrons tracks the variation of the high frequency (35 GHz) radio emission for the interval that was fit quite well, as expected for optically thin emission. Second, the temperature of the ambient plasma increases with time. With $B = 165$ G, T increases from $\sim 2 - 3 \times 10^6$ K to $\sim 8 - 10 \times 10^6$ K during the time range considered. Both T and n_{rl} depend on B : the fitted value of n_{rl} decreases and that of T increases with increasing B . Referring to Fig. 8c, we note that the fits are relatively insensitive to plasma temperature once T approaches 10^7 K (Fig. 10b) because the optical depth to free-free absorption becomes negligible. We find no evidence that the observed spectral evolution requires multiple discrete injections of electrons characterized by different energy distribution functions, as suggested by, e.g., Trottet et al. (2002), for certain events.

We checked the fitted temperature and the emission measure implied by the assumed density (i.e., $EM \sim n_{th}^2 AL$) against the GOES SXR observations for consistency (White et al. 2005). A peak temperature near 10^7 K is consistent with the GOES 0.5-4 and 1-8 Å data but the density inferred from the GOES data is perhaps a factor of two smaller than that assumed here. Given that the GOES event is very small and the uncertainties in the SXR background are relatively large, and given that the parametric fits depend on a number of assumptions, we conclude that the consistency between the fits and the SXR data is rather good.

4. Discussion

The “standard model” of flares involves energy deposition in the chromosphere by a flux of nonthermal electrons precipitating from one or more magnetic loops, resulting in heating and “evaporation” of chromospheric plasma into the corona where it emits SXR radiation. We suggest that a difference between this flare and the “standard model” is that significant chromospheric evaporation did not occur. As noted in the previous section, the spectral fits do not require an increase in the thermal plasma density during the course of the flare. Furthermore, there is a paucity of EUV and SXR emission from hot thermal plasma,

suggesting little increase in emission measure of coronal plasma and hence, little increase in the thermal plasma density.

Why is there so little chromospheric evaporation? One reason may be that the flaring loop has a large (albeit asymmetric) magnetic mirror ratio, defined as $m = B_{FP}/B_{LT} = \sin^{-2} \alpha_{lc}$, the ratio of the magnetic field strength near the magnetic footpoint to that at the loop top where the magnetic field is weakest, and α_{lc} is the loss-cone angle. A large value of m implies a small value for α_{lc} , little precipitation of energetic electrons from the loop and hence, little EUV and HXR footpoint emission. For example, a mirror ratio $m = 5$ implies only $\sim 10\%$ of an isotropic particle distribution would precipitate from the magnetic loop if magnetic trapping and weak scattering were the only relevant transport processes (e.g., Melrose & Brown 1976). A second factor is that the coronal loop, with $n_{th} = 10^{11} \text{ cm}^{-3}$, is collisionally thick to electrons with energies $\lesssim 30 \text{ keV}$ (Veronig & Brown 2004). Such electrons would deposit the bulk of their energy in the ambient plasma rather than at the loop footpoints. One might suppose that if the precipitation of energetic electrons into the footpoints is limited, thermal conduction might nevertheless drive evaporation. However, if the mirror ratio is large the footpoint area is small and evaporation due to conduction can also be strongly reduced. These considerations are consistent with the observed morphology of the HXT L band source shown in Fig. 3c. The idea of a large mirror ratio stands in contradiction to our simple model, for which a magnetically homogeneous source was assumed. This may not be a concern, however, if the magnetic loop is strongly convergent near the chromosphere (Dowdy et al. 1985).

The time interval during which plasma heating is observed via spectral fitting is from 23:10:50 to 23:11:20 UT, so that $\Delta t \approx 30 \text{ s}$. During this time, the data suggest the temperature of the ambient thermal plasma in the flaring source increased from 2-3 MK to 8-10 MK. We note that the source was presumably already heated from $\sim 0.1 \text{ MK}$ to 2-3 MK prior to the time range for which fits were computed. Whether T continued to increase significantly beyond 23:11:20 UT is not established because the model fitting becomes insensitive to temperature when $T > 10^7 \text{ K}$ although the GOES SXR emission suggest that it did not. Since both the radiative and conductive loss times are long compared to the duration of the flare, the net change of thermal energy density during the observed temperature increase is $\Delta E_{th} \approx 3n_{th}k_B\Delta T \approx 300 \text{ ergs cm}^{-3}$, yielding a mean energy deposition rate of $\dot{E} = \Delta E_{th}/\Delta t \approx 10 \text{ ergs s}^{-1} \text{ cm}^{-3}$. The magnetic energy density $u_B = B^2/8\pi \approx 1000 \text{ erg cm}^{-3}$. Hence, the energy deposition rate required to heat the plasma amounts to $\approx 1\%$ of u_B each second and a total energy deposition of $\sim 5 \times 10^{29} \text{ ergs}$.

What heats the plasma? One possibility, to which we have already alluded, is energy loss via Coulomb collisions. By virtue of its high density the coronal loop is collisionally

thick to electrons with energies $\lesssim 30$ keV. Unfortunately, no HXR observations of photon energies greater than the HXT L band are available because the flare did not trigger the *Yohkoh* flare mode. The spectral index and low-energy cutoff of the distribution of HXR-emitting electrons are unknown and hence, the number of electrons with energies of 10s of keV, cannot be inferred from the HXR observations. It may even be possible that thermal bremsstrahlung contributes to the HXT L band counts. However, if we suppose the mean energy of the HXR-emitting electrons is ≈ 30 keV, then $\approx 2 \times 10^8$ such electrons are needed each second to account for the plasma heating via collisions.

We now consider the radio-emitting electrons. The peak number density of energetic electrons with energies > 100 keV was found to be $n_{rl} \approx 10^7 \text{ cm}^{-3}$. Note that while n_{rl} is normalized to $E_0 = 100$ keV, for $B = 165$ G the bulk of the emission at radio frequencies between $\approx 10 - 40$ GHz is in fact contributed by electrons with energies of $\approx 0.7 - 3$ MeV, a result that has been previously noted (Ramaty et al. 1994, Trottet et al. 1998, 2000; Lüthi et al 2004). The energy contained in these electrons is only $\sim 0.1 \text{ ergs cm}^{-3}$, an insignificant fraction of that required to heat the ambient plasma. We conclude that the radio-emitting electrons themselves play no role in heating the plasma; but what if the power-law distribution of radio-emitting electrons extends to lower energies? The collisional energy deposition rate is

$$\dot{E} \approx \int_{E_l}^{E_C} n(E) E / t_E dE, \quad (3)$$

with

$$t_E = 170(\gamma - 1)n_{10}^{-1}\beta \approx 20E_{100}^{3/2}n_{10}^{-1} \text{ s}, \quad (4)$$

where the approximate expression for the lifetime t_E applies to mildly relativistic electrons (Melrose & Brown 1976). Here, $\gamma = 1/\sqrt{1 - \beta^2}$ is the Lorentz factor, $\beta = v/c$, E_{100} is the electron energy in units of 100 keV, and n_{10} is the thermal plasma density in units of 10^{10} cm^{-3} . Taking $\delta = 3.5$ (§3) we find $E_1 \approx 40$ keV yields an energy deposition rate of $10 \text{ ergs cm}^{-3} \text{ s}^{-1}$, in agreement with the mean energy deposition rate, and the total number of electrons $n > 40$ keV is found to be $\approx 10^8 \text{ cm}^{-3} \text{ s}^{-1}$. The inferred electron energy and number density are similar to those needed to account for plasma heating by Coulomb collisions. We conclude that the population of electrons responsible for the HXT L band emission and plasma heating can be regarded as part of the same power-law distribution of electrons responsible for the radio emission.

While this picture is appealing, it is incomplete. Thus far we have based our discussion

on the results of the two-parameter (n_{rl} , T) fits to the time series of radio spectroscopic data for which the electron energy distribution is assumed to be a power-law described by fixed values of E_o , E_c , and δ . While there are hints in the three-parameter fits of possible evolution of δ and/or E_c , such variations did not yield significantly better fits during the time interval considered. In §2.3, however, we considered the impulsive onset of the event and found that onset time progressively increased with frequency for $\nu \gtrsim 12$ GHz (Fig. 5a). The mean energy of the emitting electrons $\bar{E} \propto (\nu/\nu_B)^{0.5+0.085\delta}$ (Dulk 1985); hence, higher radio frequencies are emitted by higher energy electrons for a fixed magnetic field. The progressive delay in the onset of impulsive emission for $\nu \gtrsim 12$ GHz suggests that the more energetic the electrons, the later they appeared in the source. The onset times of emission for $\nu \lesssim 12$ GHz may at first seem inconsistent with the trend seen at higher frequencies. However, they can be understood in terms of the overall pattern of strong free-free absorption diminishing with time as the plasma temperature increases. Consider 9.4 GHz: at the time of flux onset the 9.4 GHz flux is strongly reduced by free-free absorption and Razin suppression. As the plasma heats the free-free opacity declines and the gyrosynchrotron emission increases. The triangle at 23:11:02 UT in Fig. 1b, and the dotted line in Fig. 7, indicates the time of the 35 GHz flux maximum. In Fig. 1b it clearly coincides with the "shoulder" seen in the 9.4 GHz light curve, a feature that roughly coincides with the maximum of n_{rl} . It is not until the plasma heats still further that the free-free opacity becomes negligible at 9.4 GHz and the flux maximum is achieved, well after the maximum of n_{rl} .

Therefore, despite the complicating factor of free-free absorption, we conclude that the timing delays seen in the onset of the radio emission relative to the HXT L band, and from lower to higher frequencies, are consistent with progressive acceleration of electrons with time during the impulsive rise. The net time elapsed from the acceleration of electrons with energies of 10s of keV to those with energies of 100s of keV is $\sim 2 - 3$ s, and from 100s of keV to MeV energies is $\sim 4 - 6$ s (Fig. 5a). After the initial energization to MeV energies, there does not appear to be any further significant evolution of the form electron energy spectrum, as determined by spectral fitting. We return to this point below.

Finally, we consider the observed frequency independence of the decay of the radio emission of this event, a feature shared with the flare described by White et al. (1992). This feature is clearly at odds with flare transport models in which the weak diffusion regime and magnetic trapping play a significant role (e.g., Bruggmann et al. 1994; Bastian et al. 1998; Lee et al. 2000; Kundu et al. 2001). If weak diffusion and trapping were relevant, higher energy electrons would be lost from the distribution more slowly than lower energy electrons because the collision frequency $\nu_c = 1/t_E$ and the energy loss rate decrease with energy according to equation (3). Consequently, higher frequency radio emission would decay more slowly than lower frequency emission (see Kundu et al. 2001 for a vivid example). Yet,

the radio decay profiles for the Oct 24 event are essentially identical (Fig. 5b); they are exponential with a decay time of 48 s for all frequencies with detectable emission for times later than approximately 23:11:20 UT. We conclude that while Coulomb collisions play a dominant role in the energy loss of HXR-emitting electrons (10s of keV), they do not appear to play a role in the transport of the MeV radio-emitting electrons. Instead, wave-particle interactions mediate electron transport.

To summarize our findings, electron acceleration occurs during the impulsive rise phase of the flare, progressing from energies of 10s of keV to more than an MeV in $\lesssim 10$ s. There is no compelling evidence for further significant evolution of the electron spectrum during the remainder of the flare based on model fitting. The flare plasma is collisionally thick to electrons with energies of some 10s of keV; these electrons heat the plasma. The increase in plasma temperature leads to a frequency-dependent decrease in free-free opacity, thereby explaining the increasing delay of the radio flux maximum with decreasing frequency. The decay phase of the flare at radio frequencies is incompatible with Coulomb collisions; we conclude that wave-particle interactions mediate electron transport.

Given that wave-particle interactions dominate electron transport at MeV energies, we briefly consider the role of stochastic processes for electron acceleration. Possibilities for the relevant wave modes include whistler waves (Hamilton & Petrosian 1992, Pryadko & Petrosian 1997, Petrosian & Liu 2004), fast-mode MHD waves (Miller et al. 1996), or others (see Toptygin 1985, Miller et al. 1997, for reviews). To be more concrete, consider a turbulent spectrum of whistler waves with a total energy density u_W . Hamilton & Petrosian (1992) have considered stochastic heating and acceleration by whistler waves, including the effects of Coulomb collisions. Assuming the spectral energy density of whistler wave turbulence is isotropic and can be described by a power law dependence $\propto k^{-q}$ for wave numbers $k > k_\circ$, the average pitch angle and momentum diffusion coefficients, $\langle D_{\alpha\alpha} \rangle$ and $\langle D_{pp} \rangle$, are well known (e.g., Melrose 1980, Eqns. 13 in Hamilton & Petrosian 1992). The electron mean free path is given by Hamilton & Petrosian as $\lambda = \beta c / \langle D_{\alpha\alpha} \rangle \propto (\beta\gamma)^{2-q}$. For a source of size L , taken here to be the observed loop length of $\approx 2 \times 10^9$ cm, the lifetime in the source t_s is given by $t_s = L^2 / \lambda \beta c \propto (\beta\gamma)^{q-2} / \beta$. Expressing the energy density in the turbulent spectrum relative to that in the magnetic field, $R = u_W / u_B$, we find that for the model source parameters fit in §3, λ and t_s depend on values assumed for the turbulence index q and u_W . For stochastic acceleration by whistler waves to be relevant we require $\lambda \ll L$ and $t_s \approx 50$ s. These requirements can be met when $q \sim 2$ and $R \approx 10^{-4}$. With $t_s \propto (\beta\gamma)^{q-2} / \beta$ and $q \sim 2$, λ is essentially independent of energy and t_s depends only weakly on energy. We therefore conclude that if stochastic processes in a turbulent spectrum of whistler waves are relevant, then the spectrum must be relatively flat (e.g., a Kolmogorov-like spectrum with $q = 5/3$; cf. Petrosian & Liu 2004). With the estimated turbulence level and spectrum, the

characteristic acceleration time for MeV electrons is very short, a fraction of a second. This seems to contradict the progression of delays up to ~ 6 s observed between the onset of the HXR L band emission and the radio emission. The apparent contradiction can perhaps be understood in terms of the evolution time of the turbulence spectrum. But until the specific turbulent wave mode is firmly established, and the source of the turbulence identified, it is not possible to draw any firm conclusions in this regard.

5. Summary

The flare on 2001 Oct 24 was well-observed at radio and X-ray wavelengths. It was one of the most X-ray poor events jointly observed by the HXT and the NoRP. Fortunately, comprehensive X-ray and radio observations of the event. The spatial morphology of the source is consistent with a simple coronal magnetic loop. The HXR and radio light curves revealed a progressive delay between the onset of HXT L band emission (13.9-22.7 keV) and the onset of NoRP/OVSA emission, the delay increasing with frequency for $\nu \gtrsim 12$ GHz. In contrast, the time of the maximum flux density was progressively delayed with decreasing frequency. The radio emission decay was independent of frequency.

We have modeled the flare source in terms of an admixture of nonthermal electrons and a dense thermal plasma. We suggest that the paucity of EUV, SXR, and HXR emission as a result of a relatively large mirror ratio in the magnetic loop in which the nonthermal electrons are injected/accelerated and the high ambient plasma density, which rendered the source collisionally thick to electrons $\lesssim 30$ keV. The progressive delay in the impulsive onset of radio emission with increasing frequency ($\nu \gtrsim 12$ GHz) is consistent with a progressive energization of electrons from lower to higher energies during the impulsive rise ($\lesssim 10$ s). Electrons with energies of 10s of keV deposit their energy in the coronal loop rather than at the foot points, heating the ambient plasma. The systematic plasma heating with time causes the thermal free-free absorption to decrease with time, thereby explaining the progressive delay of the radio flux maximum with decreasing frequency. The radio decay time is inconsistent with a trapping scenario. We suggest that the transport of energetic electrons is instead determined by wave-particle interactions. We suggest that the data are consistent with electron acceleration and transport mediated by a relatively flat (Kolmogorov) spectrum of whistler waves although the specifics remain an outstanding question.

We thank Hugh Hudson for comments on an early draft of this paper and the referee for useful suggestions. We are grateful to the Nobeyama Observatory for data from the NoRH and NoRP. *Yohkoh* was a mission of the Institute of Space and Astronautical Sciences in

Japan, in collaboration with the US and UK. TRACE is a NASA Small Explorer and a mission of the Stanford-Lockheed Institute for Space Research. We acknowledge use of a magnetogram from the Kitt Peak National Observatory and an $H\alpha$ filtergram from the Big Bear Solar Observatory. The National Radio Astronomy Observatory is a facility of the National Science Foundation operated under cooperative agreement by Associated Universities, Inc. GDF acknowledges that this work was supported in part by the Russian Foundation for Basic Research, grants 06-02-16295a and 06-02-16859a. DEG acknowledges that this work was supported in part by NSF grant AST-0607544 and NASA grant NNG06GJ40G to the New Jersey Institute of Technology.

REFERENCES

- Bai, T., & Ramaty, R. 1976, *Sol. Phys.*, 49, 343
- Bai, T., & Ramaty, R. 1979, *ApJ*, 227, 1072
- Bastian, T.S., Benz, A.O., & Gary, D.E. 1998, *ARAA* 36, 131
- Bastian, T. S. 1999, in *Solar Physics with Radio Observations*, Proc. Nobeyama Symposium, eds. T. S. Bastian, N. Gopalswamy, & K. Shibasaki, NRO Report 479, p. 211
- Belkora, L. 1997, *ApJ*, 481, 532
- Benka, S. G., & Holman, G. D. 1992, *ApJ*, 391, 854
- Bespalov, P. A., Zaitsev, V. V., & Stepanov, A. V. 1991, *ApJ*, 374, 369
- Dowdy, J. F., Jr., Moore, R. L., & Wu, S. T. 1985, *Sol. Phys.*, 99, 79
- Dulk, G. A. 1985, *ARA&A*, 23, 169
- Fleishman, G.D., & Melnikov, V.F. 2003, *ApJ*, 587, 823
- Gary, D. E., & Hurford, G. J. 1994, *ApJ*, 420, 903
- Ginzburg, V. L., & Syrovatskii, S. I. 1969, *ARAA* 7, 375
- Handy, B. N., Acton, L. W., Kankelborg, C. C., Wolfson, C. J., Akin, D. J., et al. 1999, *Sol. Phys.*, 187, 229
- Hamilton, R. J., & Petrosian, V. 1992, *ApJ*, 398, 350
- Hudson, H., & Ryan, J. 1995, *ARA&A*, 33, 239

- Kai, K., Kosugi, T., & Nitta, N. 1985, PASJ, 37, 155
- Klein, K.-L. 1987, A&A, 183, 341
- Kosugi, T., Dennis, B. R., & Kai, K. 1988, ApJ, 324, 1118
- Kosugi, T., et al. 1992, PASJ, 44, L45
- Kundu, M. R., White, S. M., Gopalswamy, N., & Lim, J. 1994, ApJS, 90, 599
- Kundu, M. R., Nindos, A., & Grechnev, V. V. 2004, A&A, 420, 351
- Lang, K. R. 1980, A Compendium for the Physicist and Astrophysicist, XXIX, 783 pp. Springer-Verlag Berlin Heidelberg New York.
- Lee, J., Gary, D. E., & Shibasaki, K. 2000, ApJ, 531, 1109
- Lee, J., Gallagher, P.T., Gary, D.E., Nita, G.M., Choe, G.S., Bong, S.C., & Yun, H.S. 2003, ApJ, 585, 524
- Lim, J., White, S. M., Kundu, M. R., & Gary, D. E. 1992, Sol. Phys., 140, 343
- Melnikov, V., & Magun, A. 1998, Sol. Phys., 178, 153
- Melnikov, V. F., Gary, D. E., & Nita, G. M. 2007, ApJ, submitted
- Melrose, D. B., & Brown, J. C. 1976, MNRAS, 176, 15
- Miller, J. A., Larosa, T. N., & Moore, R. L. 1996, ApJ, 461, 445
- Miller, J. A. 1997, ApJ, 491, 939
- Miller, J. A., et al. 1997, J. Geophys. Res., 102, 14631
- Nakajima, H., Enome, S., Shibasaki, S., Nishio, M., Takano, T., et al. 1994, *Proc. Inst. Electr. Electron. Eng.* 82, 705
- Nindos, A., White, S. M., Kundu, M. R., & Gary, D. E. 2000, ApJ, 533, 1053
- Nita, G. M., Gary, D. E., & Lee, J. 2004, ApJ, 605, 528
- Orwig, L. E., Frost, K. J., & Dennis, B. R. 1980, Sol. Phys., 65, 25
- Petrosian, V., & Liu, S. 2004, ApJ, 610, 550
- Press, W. H., Flannery, B. P., & Teukolsky, S. A. 1986, Cambridge: University Press, 1986

- Pryadko, J. M., & Petrosian, V. 1997, *ApJ*, 482, 774
- Razin, V. A. 1960, *Izv. VUZov Radiofizika* 3, 584
- Ramaty, R. 1969, *ApJ*, 158, 753
- Ramaty, R., & Petrosian, V. 1972, *ApJ*, 178, 241
- Rieger, E., & Marschhäuser, H. 1991, *Max '91/SMM Solar Flares: Observations and Theory*, 68
- Sato, J., et al. 2006, *Sol. Phys.*, 236, 351
- Silva, A. V. R., Wang, H., & Gary, D. E. 2000, *ApJ*, 545, 1116
- Takakura, T., Ohki, K., Kosugi, T., Enome, S., & Degaonkar, S. S. 1983, *Sol. Phys.*, 89, 379
- Toptygin, I.N. 1985, *Cosmic rays in interplanetary magnetic fields* (Dordrecht, D. Reidel)
- Trottet, G., Vilmer, N., Barat, C., Benz, A., Magun, A., Kuznetsov, A., Sunyaev, R., & Terekhov, O. 1998, *A&A*, 334, 1099
- Trottet, G., Rolli, E., Magun, A., Barat, C., Kuznetsov, A., Sunyaev, R., & Terekhov, O. 2000, *A&A*, 356, 1067
- Trottet, G., Raulin, J.-P., Kaufmann, P., Siarkowski, M., Klein, K.-L., & Gary, D. E. 2002, *A&A*, 381, 694
- White, S. M., Thomas, R. J., & Schwartz, R. A. 2005, *Sol. Phys.*,
- Veronig, A.M., & Brown, J.C. 2004, *ApJ*, 603, L117
- Yoshimori, M., et al. 1992, *PASJ*, 44, L51
- White, S. M., Kundu, M. R., Bastian, T. S., Gary, D. E., Hurford, G. J., Kucera, T., & Bieging, J. H. 1992, *ApJ*, 384, 656

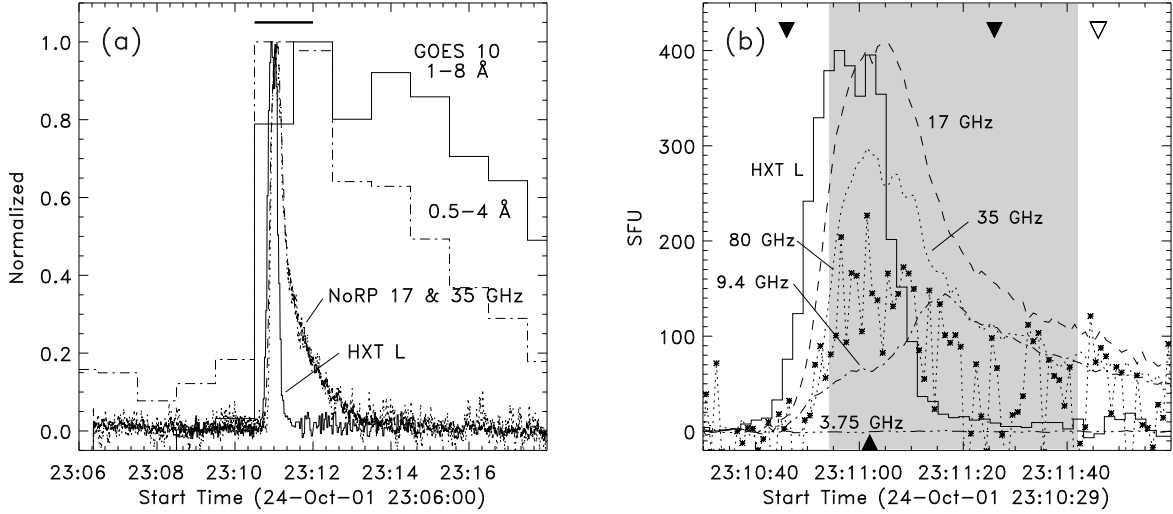


Fig. 1.— a) Overview of the radio and X-ray emission from the flare that occurred at 23:11 UT on 2001 October 24. The *Yohkoh* HXT L band (13.9-22.7 keV) photon counts, the GOES 10 0.5-4Å and 1-8Å SXR fluxes averaged to 1 min, and the NoRP 17 and 35 GHz emissions are shown. Each trace is normalized to its maximum. b) Detail of the NoRP and HXT L observations, corresponding the time range indicated by the horizontal bar at the top of panel (a). The radio flux densities are indicated by the ordinate label. The HXT L band background-subtracted counts (solid line; maximum of 6 cts sc⁻¹ s⁻¹) have been scaled for ease of comparison. The solid inverted triangles indicate the times of the TRACE 171 Å images. The open inverted triangle indicates the time the single SXT full disk image (AlMg filter). The shaded area indicates the time range for which model fits to the radio spectroscopic data were obtained (see §3.2).

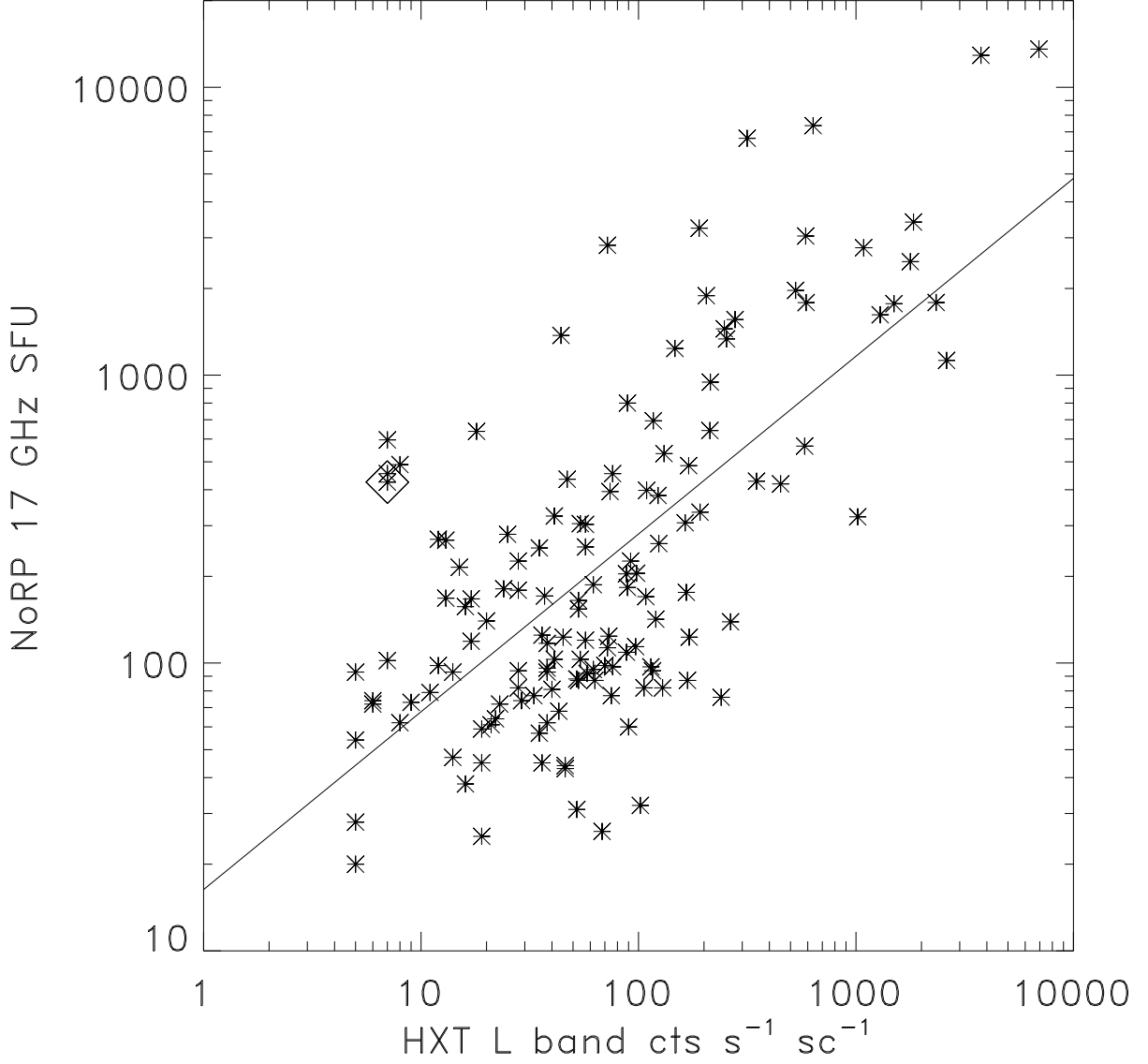


Fig. 2.— Plot of the NoRP 17 GHz flux versus the *Yohkoh* HXT L band (13.9–22.7 keV) count rate for the 135 flares coincident to 10 min and observed jointly by the two instruments during the lifetime of the *Yohkoh* mission. Only events above 20 SFU at 17 GHz and 4 cts $\text{s}^{-1} \text{sc}^{-1}$ in the HXT L band are shown. The flare of 2001 October 24 is indicated by the diamond symbol.

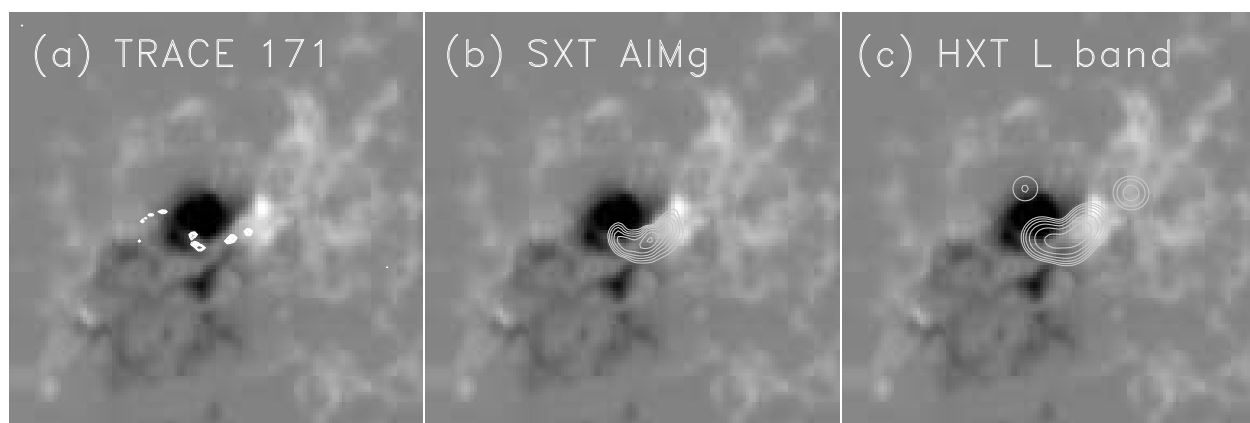


Fig. 3.— A comparison of TRACE, SXT, and HXT maps and a KPNO magnetogram. a) A difference map formed from TRACE 171 Å images obtained at 23:10:05 UT and 23:11:26 UT; b) The SXT image detail obtained from the full disk image at 23:11:46 UT with the AlMg filter. b) The HXT L band (13.9–22.7 keV) map using counts accumulated for the duration of the impulsive spike.

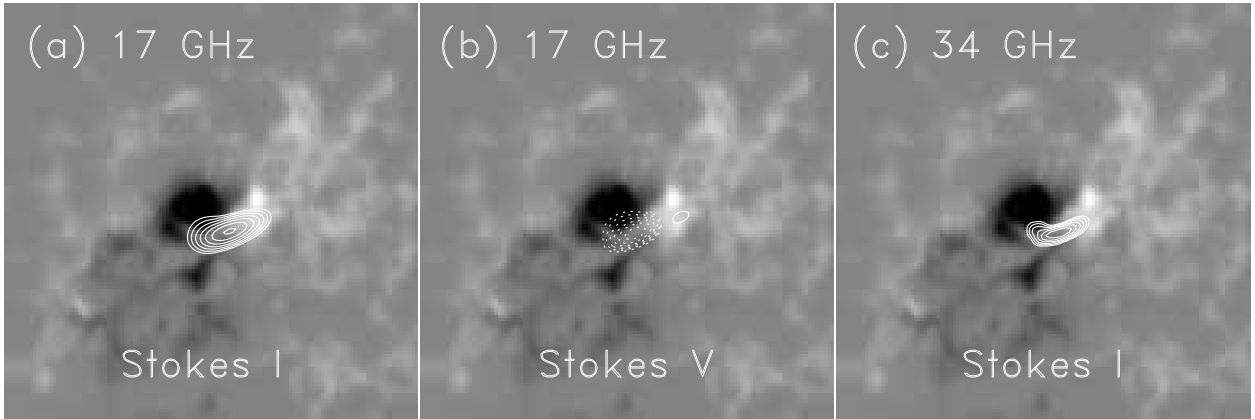


Fig. 4.— A comparison of the NoRH maps with the KPNO magnetogram. a) The map of the 17 GHz total intensity (Stokes I parameter) at the time of 17 GHz flux maximum (23:11:10 UT). The maximum brightness temperature is 4.6×10^7 K. The contour levels are at intervals of $\sqrt{2}$ from 12% to 96% of the maximum. b) The map of the 17 GHz circularly polarized intensity (Stokes V parameter) at the time of the 17 GHz total intensity maximum. The contour levels are again 12% to 95% of the maximum at intervals of $\sqrt{2}$; c) The map of the 34 GHz total intensity at the time of the 17 GHz maximum. The maximum brightness temperature is 1.8×10^7 K. The contour levels are again 12% to 95% of the maximum brightness.

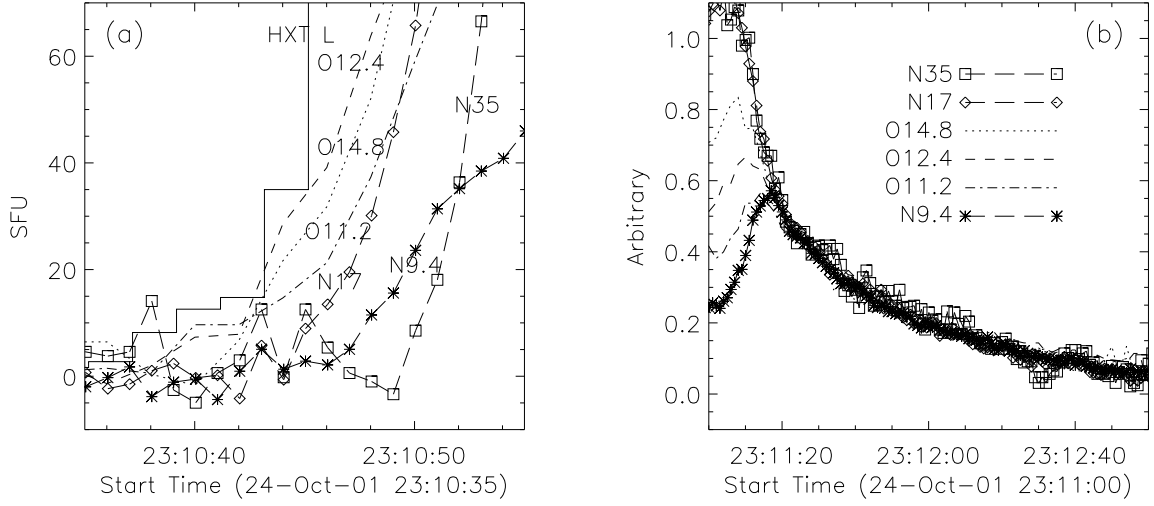


Fig. 5.— a) Detail of the impulsive rise of the burst comparing the HXT L band and selected NoRP and OVSA frequencies. b) Detail of the decay phase. The NoRP and OVSA frequencies shown in panel (a) have been scaled to emphasize that the decay rate of each is essentially identical after 23:11:20 UT. The delay in the flux maximum as a function of decreasing frequency is also evident.

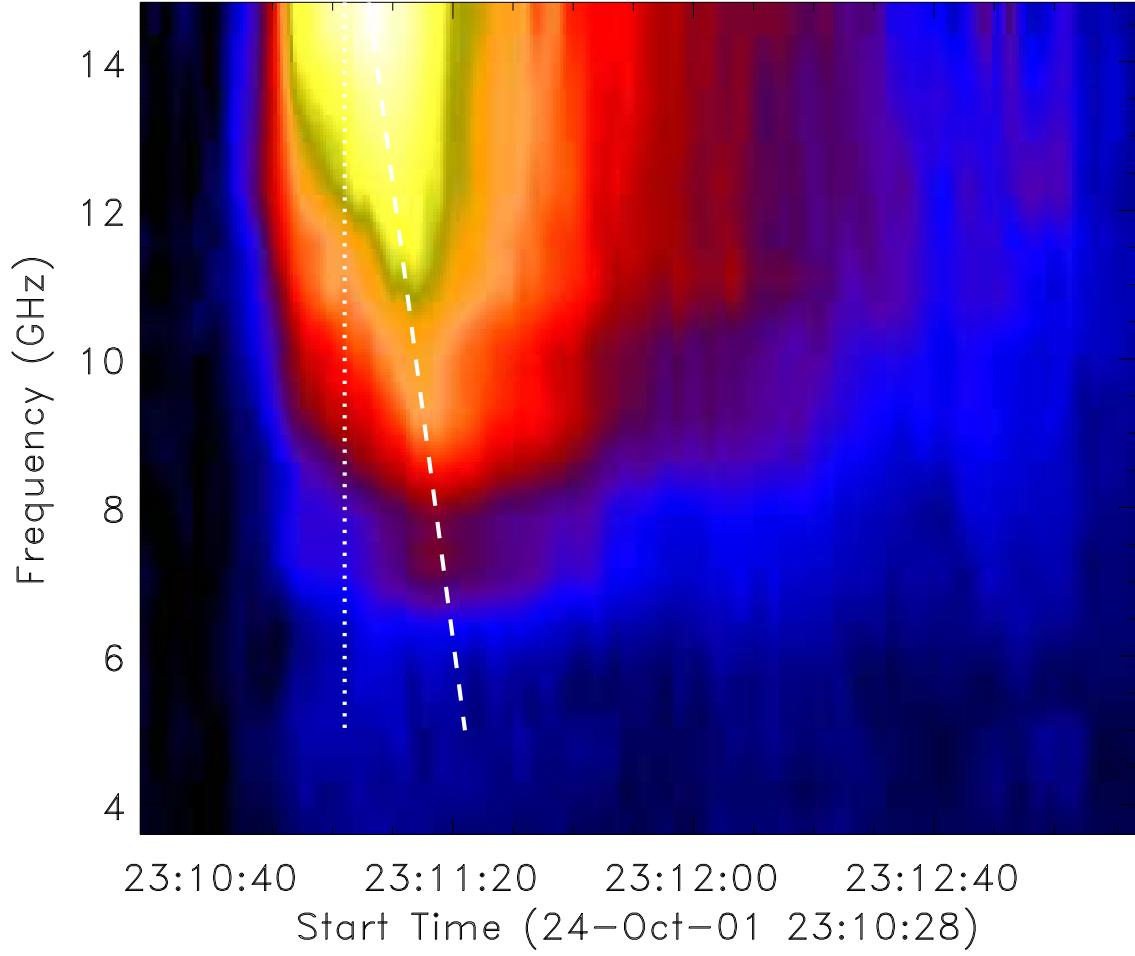


Fig. 6.— A dynamic spectrum of the OVSA data. The dashed line emphasizes the increasing time of the flux maximum as a function of decreasing frequency. The dotted vertical line indicates the time of the 35 GHz flux maximum.

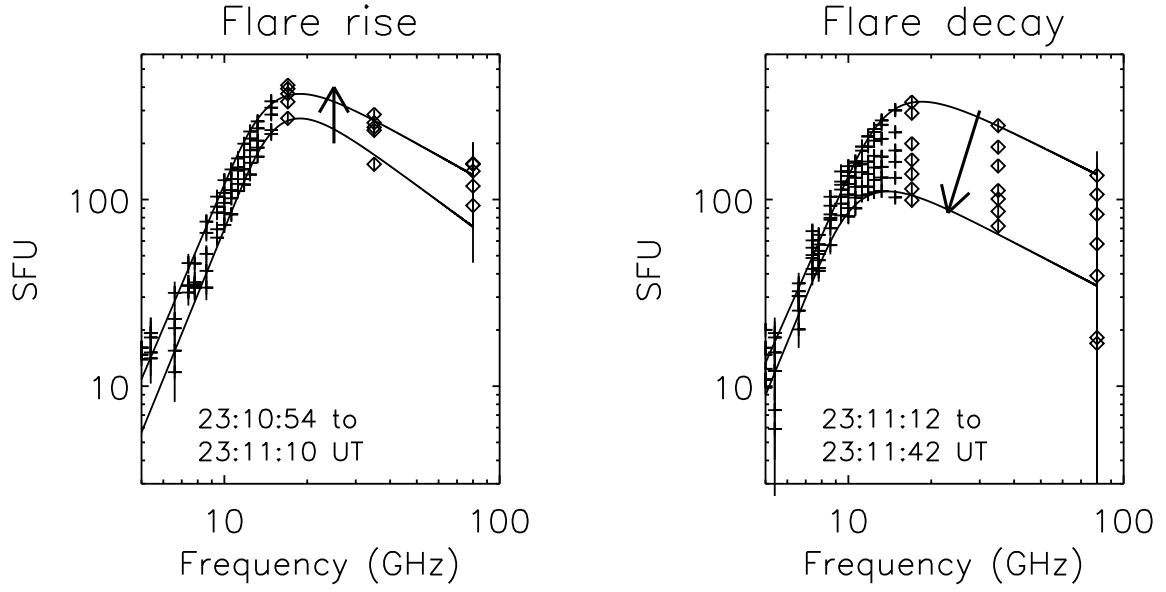


Fig. 7.— Stack plots of composite spectra shown using OVSA data (asterisks) and NoRP data (squares) during (a) the flare rise phase, during which spectra are shown at 4 s intervals; b) the flare decay, during which spectra are shown at 6 s intervals.

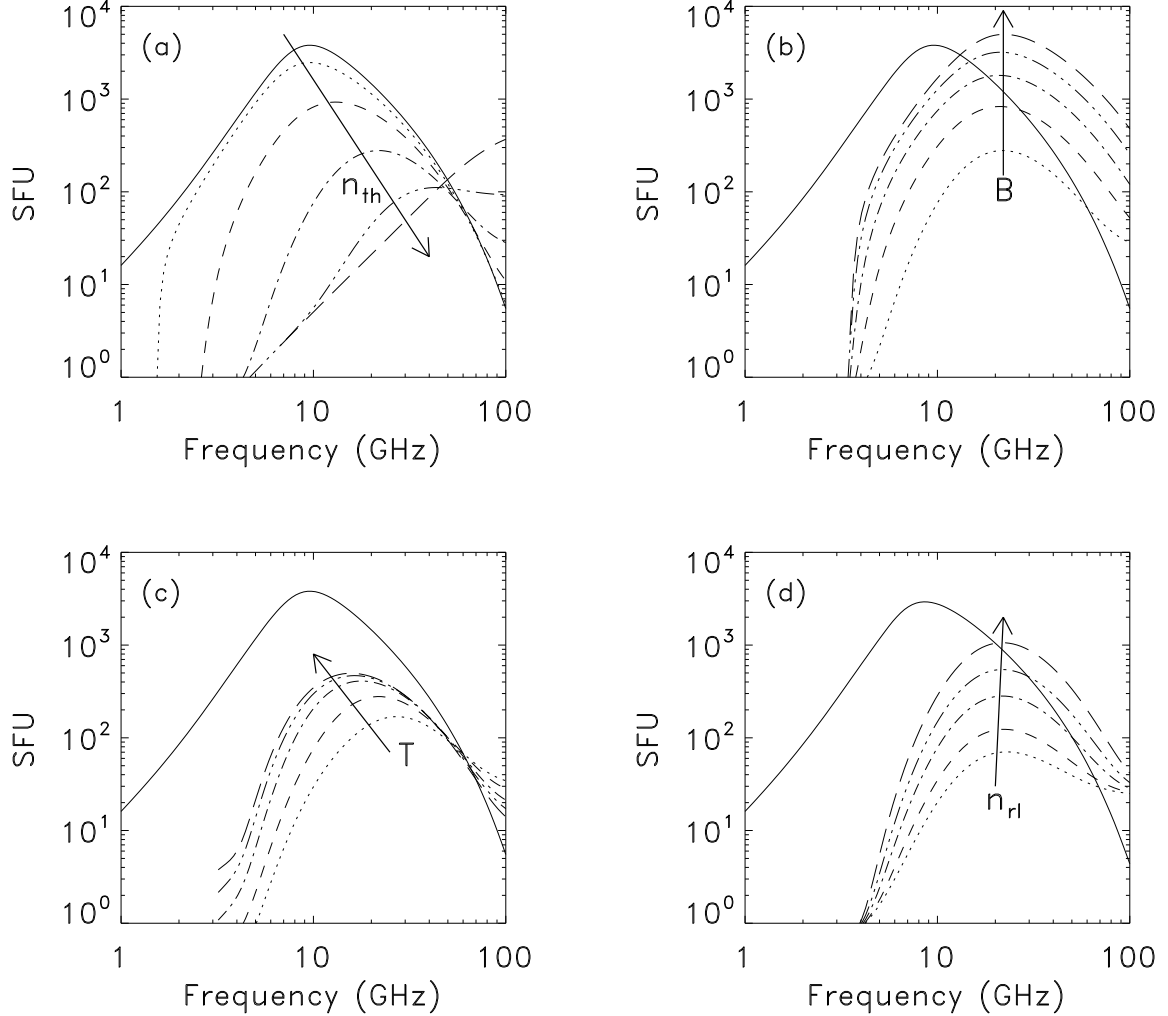


Fig. 8.— Gyrosynchrotron spectra computed to illustrate parameter dependencies. In all cases, the solid line represents gyrosynchrotron emission from electrons *in vacuo* and by parameters given in the text. a) variation of the spectrum when a background thermal plasma with a temperature $T = 2 \times 10^6$ K is present: dotted line: $n_{th} = 2 \times 10^{10} \text{ cm}^{-3}$; dashed line: $n_{th} = 5 \times 10^{10} \text{ cm}^{-3}$; dot-dash: $n_{th} = 2 \times 10^{11} \text{ cm}^{-3}$; dot-dot-dot-dash: $n_{th} = 2 \times 10^{11} \text{ cm}^{-3}$; long-dash: $n_{th} = 5 \times 10^{11} \text{ cm}^{-3}$; b) same, except $n_{th} = 10^{11} \text{ cm}^{-3}$, $n_{rl} = 5 \times 10^6 \text{ cm}^{-3}$, $T = 2 \times 10^6$ K, and $B = 150, 200, 250, 300, 350$ G, respectively; c) same as (b) except $B = 150$ G and $T = 10^6, 2 \times 10^6, 5 \times 10^6, 10^7$, and 2×10^7 K, respectively; d) same as (c) except $T = 2 \times 10^6$ and $n_{rl} = 10^6, 2 \times 10^6, 5 \times 10^6, 10^7, 2 \times 10^7 \text{ cm}^{-3}$, respectively.

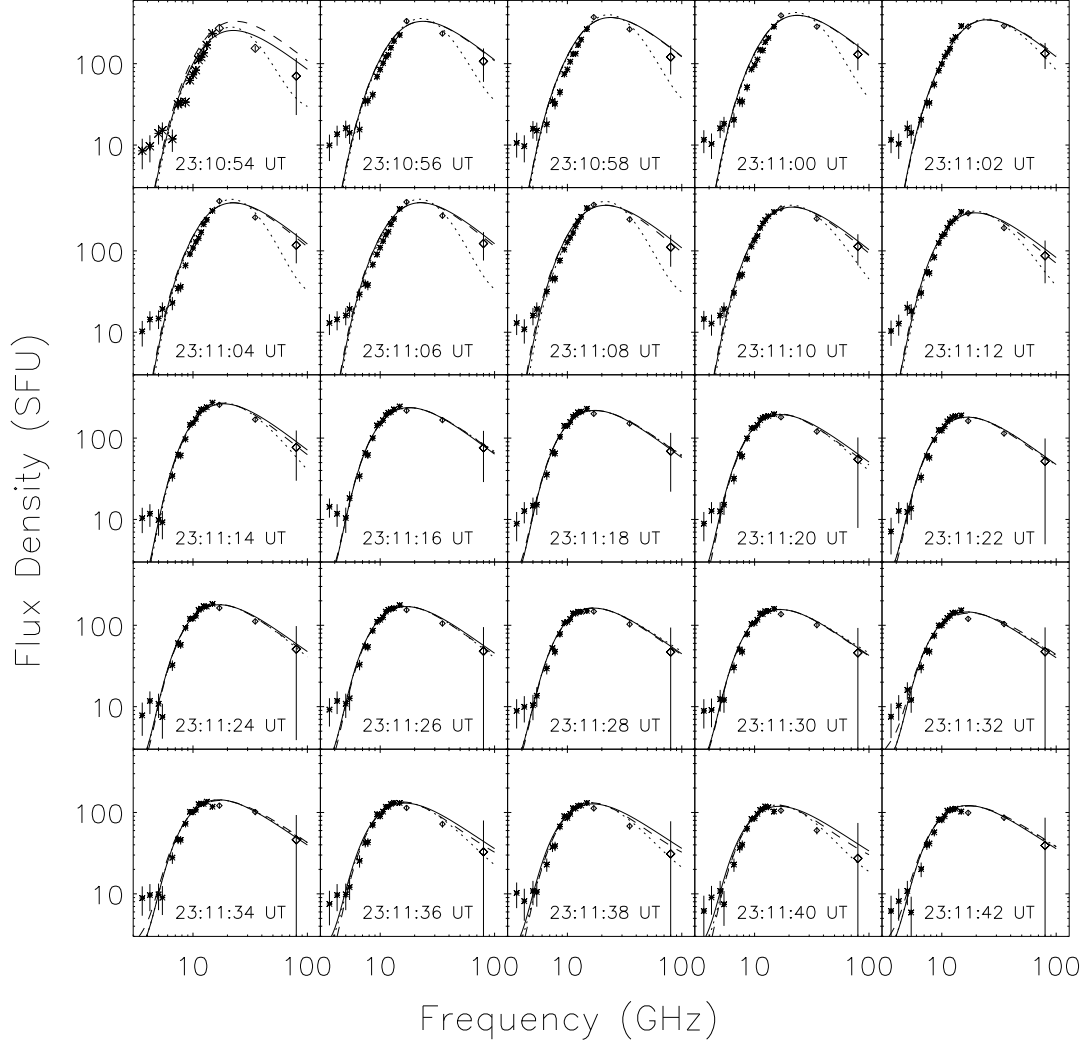


Fig. 9.— Time sequence of radio spectra and model fits are shown with two-parameter (solid line) and three-parameter (dashed lines) fits. See the text for details.

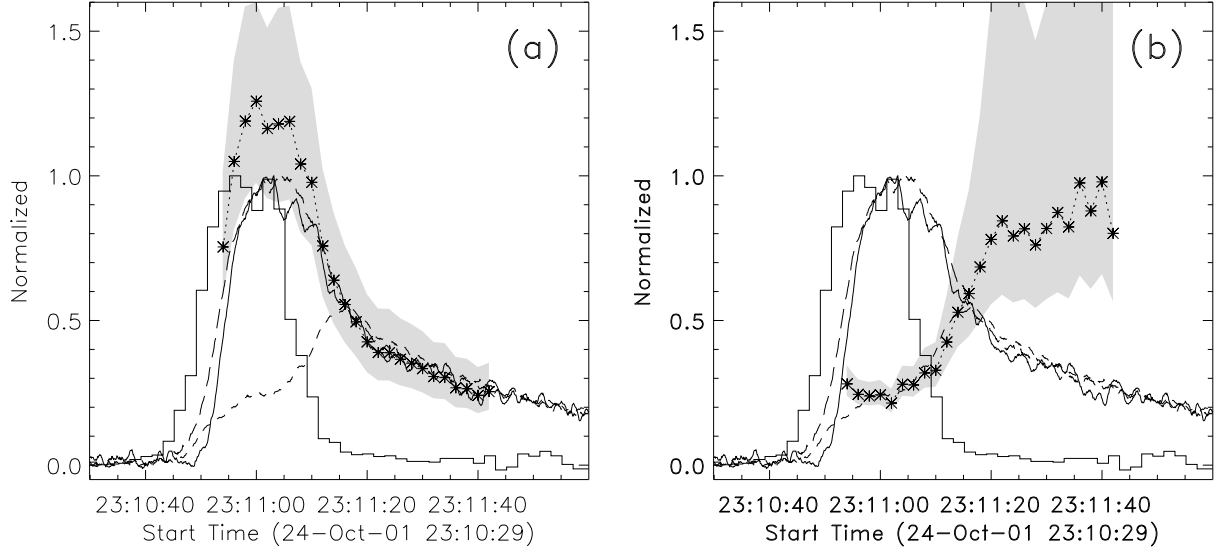


Fig. 10.— a) The variation of n_{rl} with time in comparison to the HXT L band (thin solid line) and radio emission at 9.4 (short dashes), 17 (long dashes), and 35 GHz (heavy solid line). The HXR and radio data have been normalized to their respective maxima. The dotted line connecting asterisks shows the variation of the fitted value of n_{rl} (divided by 10^7 cm^{-3}) for an assumed magnetic field strength of 165 G in the source. The shaded area indicates the range of n_{rl} for assumed magnetic field strengths of 150 and 180 G. b) The same as panel (a), except the asterisks show the variation of the fitted value of the temperature T (divided by 10^7 K) of the ambient plasma for an assumed magnetic field strength of 165 G in the source. The shaded area indicates the temperatures when the magnetic field is 150 and 180 G.